



**HAL**  
open science

## Characterization of time-varying regimes in remote sensing time series: application to the forecasting of satellite-derived suspended matter concentrations

Bertrand Saulquin, Ronan Fablet, Pierre Ailliot, Grégoire Mercier, David Doxaran, Antoine Mangin, Odile Fanton d'Andon

### ► To cite this version:

Bertrand Saulquin, Ronan Fablet, Pierre Ailliot, Grégoire Mercier, David Doxaran, et al.. Characterization of time-varying regimes in remote sensing time series: application to the forecasting of satellite-derived suspended matter concentrations. *IEEE Journal of Selected Topics in Applied Earth Observations and Remote Sensing*, 2014, 8 (1), pp.406 - 417. 10.1109/JSTARS.2014.2360239 . hal-01188636

**HAL Id: hal-01188636**

**<https://hal.science/hal-01188636v1>**

Submitted on 12 Oct 2015

**HAL** is a multi-disciplinary open access archive for the deposit and dissemination of scientific research documents, whether they are published or not. The documents may come from teaching and research institutions in France or abroad, or from public or private research centers.

L'archive ouverte pluridisciplinaire **HAL**, est destinée au dépôt et à la diffusion de documents scientifiques de niveau recherche, publiés ou non, émanant des établissements d'enseignement et de recherche français ou étrangers, des laboratoires publics ou privés.

1        **Characterization of time-varying regimes in remote sensing time**  
2        **series: application to the forecasting of satellite-derived suspended**  
3        **matter concentrations**

4        Bertrand Saulquin (1, 2), Ronan Fablet (2, 3), Pierre Ailliot (3), Grégoire Mercier (2, 3), David  
5        Doxaran (4), Antoine Mangin (2), Odile Fanton d'Andon (2).

6        (1)    ACRI-ST,    Sophia-Antipolis,    260    route    du    Pin    Montard,    BP    234  
7        06904 Sophia-Antipolis, France

8        (2)    Institut Mines-Telecom, Télécom Bretagne; UMR CNRS 3192 Lab-STICC, Technopôle  
9        Brest Iroise CS 83818, 29238 Brest, France

10       (3)    Université Européenne de Bretagne, 35000 Rennes, France

11       (4)    CNRS, Université Pierre et Marie Curie-Paris 6, UMR 7093, Laboratoire d'Océanographie  
12       de Villefranche/Mer, 06230 Villefranche-sur-Mer, France

13       Corresponding author: [bertrand.saulquin@acri-st.fr](mailto:bertrand.saulquin@acri-st.fr)

14       Submission date: 19/05/2014

15       ***Abstract***

16  
17       Satellite data, with their spatial and temporal coverage, are particularly well suited for the  
18       analysis and characterization of space-time-varying relationships between geophysical processes. In  
19       this study, we investigate the forecasting of a geophysical variable using both satellite observations  
20       and model outputs. The studied latent-regime models **aim here at** identifying time-varying regime

21 shifts within a dataset which is a key of interest for geophysical processes driven by the seasonal  
22 variability. As a specific example, we study the daily concentration from 2007 to 2009 of mineral  
23 suspended particulate matters estimated from the satellite-derived MODIS, MERIS and SeaWiFS  
24 dataset, in coastal waters adjacent to the Gironde River mouth (South West of France). We clearly  
25 show that the forecast of the high resolution suspended particulate matter dataset using  
26 environmental data (wave height, wind strength and direction, tides and river outflow) and a multi-  
27 regime model is significantly improved compared with a classical multi-regression and a Support  
28 Vector Regression model. Each regime is here characterized by a regression function and a  
29 covariance structure.

30 From an analytical point of view, we compare the results obtained with four models:  
31 homogeneous and non-homogeneous Markov-switching models, with and without an  
32 autoregressive term, i.e. the suspended matter concentration observed the day before. Inclusion of  
33 an autoregressive term is motivated by the strong natural autocorrelation level depicted by  
34 geophysical time series, but, one may avoid this term if, for example, the observations are no more  
35 available during specific conditions or periods. With the evaluated models, best results are obtained  
36 with a mixture of 3 regimes for both autoregressive and non-autoregressive models. Prediction  
37 performance at day+1, using the non-autoregressive models and a validation dataset, reached 80%  
38 of the observed variance, compared to 32% for a standard single-regime (regression) analysis, and  
39 40 % for a Support Vector Regression. Inclusion of an autoregressive term increases results to 93%  
40 of explained variance for the mixture model compared to 80% without autoregressive term and 85%  
41 using a Support Vector Regression. These results stress the potential of the identification of  
42 geophysical regimes to improve the forecasting, or the inversion, of a high resolution geophysical  
43 variable using both observations and model outputs. We also show that for short periods of lack of  
44 observations (less than 15 days), estimations using the autoregressive term are better than without.  
45 In this case the autoregressive term and the transition probabilities between regimes are estimated  
46 using available model outputs.

47 Index term: 1) Satellite-derived suspended matter time series analysis. 2) Statistical forecasting. 3)  
48 Regime-switching latent regression models. 4) Joint analysis of satellite-derived products and  
49 operational model outputs. 5) Gironde river plume.

## 50 **1 Introduction**

51

52 The forecasting of a geophysical variable using statistical models is an alternative to model-  
53 based approaches which typically involve complex simulation and/or assimilation [1, 2]. For  
54 instance, coupled hydrodynamic and sediment transport models can be used to estimate the  
55 concentration of suspended particulate matters within the water column [3] while statistical  
56 approaches may use available satellite and model data to predict the same variable [4]. Many  
57 statistical approaches have been proposed and evaluated to forecast or infer a studied variable from  
58 predictors. Among them, linear multivariate regression [5] and non-linear (polynomial) multivariate  
59 regression [6] are the most known. Numerous specific models dedicated to time-series analysis such  
60 as AutoRegressive Moving Average (ARMA) and AutoRegressive Integrated Moving Average  
61 (ARIMA) models [7] have also been developed initially to address financial time series. **These**  
62 **latest**, which aim at studying the behavior of a time series without considering forcing factors, have  
63 also been applied to geophysical time series [8]. Non-linear regressions, based on supervised  
64 learning strategies, such as Neural Networks [9] and Support Vector Regressions (SVR) [10] may  
65 provide relevant alternatives to estimate a variable from predictors. In the context of geophysical  
66 studies, they may nevertheless suffer from two major drawbacks. First, though relevant regression  
67 performances may be reported, these models are not physically interpretable and may be very  
68 sensitive to the training dataset. Second, multi-regime dynamics, often exhibited by geophysical  
69 processes driven by the seasonality [11], cannot be addressed by **non-linear models**, contrary to  
70 latent-regime models as demonstrated in our study.

71 We propose here to characterize time-varying relationships between a variable and its forcing  
72 parameters using latent-regime models, and hence optimize forecasting results. As an illustration,  
73 we address the concentration of inorganic suspended particle matters (SPIM), estimated from  
74 satellite data using a regional algorithm [12, 13], and observed in the mouth of the Gironde estuary.  
75 In this area, sediments are mainly exported from the Gironde estuary [13, 14] and SPIM  
76 concentration clearly depends on the local physical forcing: swell, tide, wind and river discharge. A  
77 minimum of energy has to be brought by waves and tides to re-suspend cohesive sediments  
78 accumulated at the bottom. Conversely, when sediments have been re-suspended in the water  
79 column by wave influence, their settling velocity depends on their size and density [15] and  
80 physico-chemical properties [16]. This example stresses that the relationships between the studied  
81 variable (SPIM) and the causing factors evolve in space and time and potentially requires advanced  
82 statistical methods to identify the underlying geophysical regimes.

83 From a methodological point of view, “latent regime regressions” also referred as “clusterwise  
84 regressions” [17, 18] are particularly appealing to identify such non-linear and multi-regime  
85 patterns within a dataset. Each regime is associated with a linear regression and a non-linear  
86 relationship is thus estimated as a sum of linear contributions. Regarding the temporal dynamics of  
87 these regimes, we here consider Markovian processes [19], which state the transitions in time  
88 between two regimes. The standard Hidden Markov Model (HMM) and Non-Homogeneous  
89 Markov Model (NHMM) are evaluated [19]. The inclusion of an autoregressive term (HMM-AR)  
90 and (NHMM-AR) is also discussed. This aspect is motivated on the one hand by the strong  
91 autocorrelation level depicted by geophysical time series [20]. When the observation at  $t-1$  is  
92 available, it is obvious, considering the strong natural autocorrelation of geophysical data that the  
93 forecast at time  $t$  should take into account the observation at time  $t-1$ . Conversely, for specific  
94 applications, or if the observations are not available during long periods (such as winter storms, or  
95 after a sensor failure), one may need to estimate the variable without using the observations of the

96 previous days. We discuss here the choice between autoregressive or not autoregressive models for  
97 long lack of observation period using forecasting results from  $t+1$  to  $t+15$ .

98 Model parameter estimation is carried out from a dataset composed of 5862 time series of 1096  
99 points in the mouth of the Gironde estuary in the  $[3^{\circ}\text{W}-1^{\circ}\text{E} ; 45-46.5^{\circ}\text{N}]$  area during the period  
100 2007-2009. Validation is performed on the same area for using the data for the year 2010. We used  
101 EOFs to reduce the dimension of the space-time observations. This is a usual approach in spatio-  
102 temporal statistics [21, 22] although alternatives may be considered such as linear discriminant  
103 analysis [23], and, we could also introduce a latent variable to describe the regime at each location  
104 and interact with the regimes at other locations. Nevertheless, such models are known to be very  
105 difficult to fit on the data and remain a research challenge for statisticians. We infer our mixture  
106 model using the expansion coefficients of the first four modes of the EOF which explain 99% of the  
107 total variance. The variables used as predictors for the SPIM expansion coefficients (EC) are the  
108 wave height issued from a numerical model [24], the wind fields optimally interpolated from  
109 satellite observations [25], the tide coefficient [26] and the Gironde fresh water discharge (sum of  
110 the Garonne and Dordogne Rivers contributions).

## 111 **2 Methods**

### 112 **2.1 Markov switching forecast models**

113

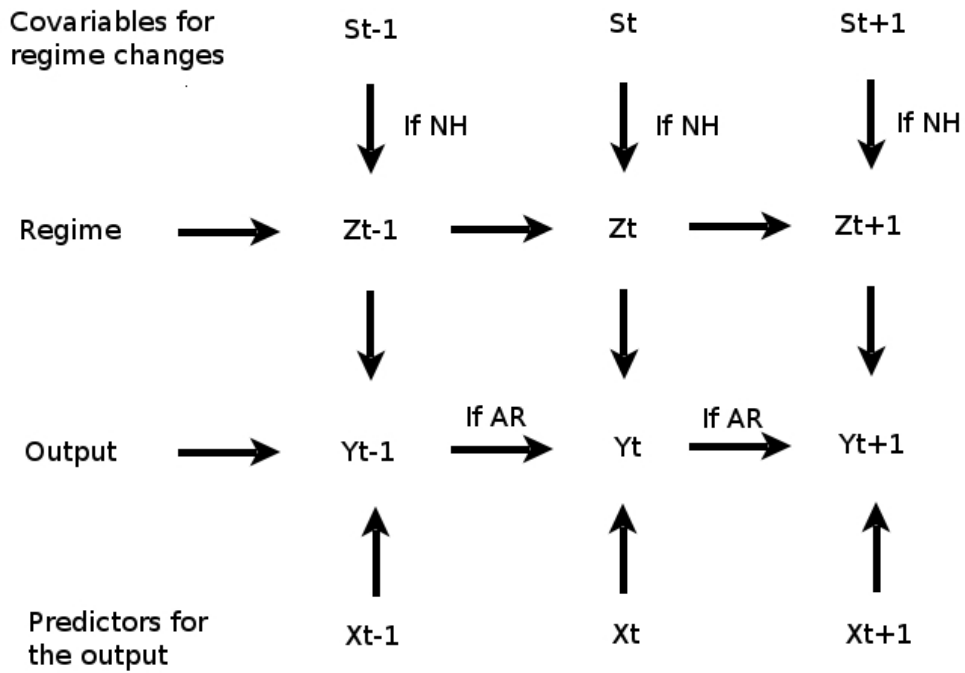
114 We address here the study of a two dimensional scalar geophysical time series  $Y$ . In a hidden  
115 Markov model framework (HMM; [19]), one states two different processes, the observed process  $Y$   
116 and a hidden process  $Z$ . The observed process (here the turbidity) is assumed to be temporally  
117 dependent of the hidden process. The hidden process  $Z_t$  is modeled as a first order Markov chain  
118 [19]. At a given time  $t$ , the hidden variable  $Z_t = k$  is a discrete value which states the regime

119 characterized by a latent [17] regression model with coefficient  $B_k$  between the variable  $Y_t$  and the  
120 predictor  $X_t$ . At time  $t$ , knowing regime variable  $Z_t$ , the observed variable  $Y_t$  is modeled as:

$$121 \quad (Y_t | Z_t=k) = X_t B_k \quad (1)$$

122 where  $X_t B_k$  is the regression function, which predicts variable  $Y_t$  from some predictors  $X_t$  for  
123 regime  $Z_t = k$ .

124 Figure 1 shows a graphical representation of the conditional dependencies involved in the  
125 model, in the form of the general Directed Acyclic Diagram (DAG). It illustrates the interactions  
126 between the variable  $Y_t$ , the predictors  $X_t$ , the hidden regime  $Z_t$  and the covariate  $S_t$  which acts on  
127 regime switching.  $X_t$  may contain lagged values of  $Y_t$  (referred as autoregressive terms) and/or  
128 exogenous covariates such as wind or wave height. Figure 1 defines a general family of model  
129 which encompasses the most usual ones with regime switching. When no covariate is considered  
130 i.e.,  $Z_t$  only depends  $Z_{t-1}$ , and,  $Y_t$  only depends on  $(Y_{t-s} \dots Y_{t-1})$  and  $Z_t$ , we retrieve the usual Markov  
131 switching autoregressive (MS-AR). If we further assume that  $s=0$  (without autoregressive  
132 component where  $Y_t$  only depends on  $Z_t$ ) then we obtain the Hidden Markov Models (HMMs).  
133 When  $Z_t$  does not depend on  $Z_{t-1}$ , and the dependence on  $S_t$  is parameterized using indicator  
134 functions, we obtain the threshold autoregressive (TAR) model which is the other important family  
135 with regime switches in the literature. HMMs, MS-AR and TAR have been used in many fields of  
136 applications including geosciences [27].



137

138 Figure 1: Graphical representation of the various Markov-Switching Models considered in this  
 139 work: the arrows state the conditional dependencies between the random processes in play, namely  
 140 hidden regime process  $Z$ , observed process  $Y$ , prediction process  $X$  and regime change covariate  
 141 process  $S$ .

142 In the following equations (2 to 14),  $X_t$  and  $S_t$  are known, as they are either observations or  
 143 numerical model outputs. Given (1) the conditional likelihood of the observation  $Y_t$  given  
 144 predictors  $X_t$  and regime  $Z_t$  is expressed as [17]:

$$145 \quad P_{Y_t|X_t, Z_t=k} \sim N(X_t B_k, \sigma_k) \quad (2)$$

146 where  $N$  represents the Gaussian probability density function with mean  $X_t B_k$  and covariance  
 147  $\sigma_k$ . Hence, given predictors up to time  $t$  we can predict process  $Y$  from its expectation conditionally  
 148 to process  $X$ :



149 
$$Y_t = E Y_t | X_t = k = \frac{1}{K} \sum_{l=1}^K P(Z_t = l | X_t) E Y_t | Z_t = l, X_t = k = \frac{1}{K} \sum_{l=1}^K P(Z_t = l | X_t) \mu_{lk} \quad (3)$$

150 where  $K$  is the number of regimes.  $P(Z_t = k | X_t) = \pi_{tk}$  is the posterior probability that the  
 151 dynamical regime  $Z$  at time  $t$  is of type  $k$  [17].

### 152 **3 Markov-switching priors**

153

154 Stating hidden regime process  $Z$  as a first-order Markovian process amounts to modeling the  
 155 transition between successive regimes at time  $t$  and time  $t-1$ . In the simplest case, one assumes  
 156 homogeneous transitions, i.e. time-independent and context-independent transitions, and the  
 157 Markovian process is fully characterized by its transition matrix  $P(Z_t = k | Z_{t-1} = l)$  for possible pairs  
 158 of successive regimes  $(k, l)$ . In the HMM setting the conditional distribution of  $Z_t$ , given the past  
 159 values  $Y_s$  and  $Z_s$  for  $s < t$ , is assumed to depend only on  $Z_{t-1}$  (Fig. 1):

160 
$$\pi_{tk} = P(Z_t = k | Y_0, \dots, Y_t) = \frac{1}{K} \sum_{l=1}^K P(Y_t | Z_t = k) P(Z_t = k | Z_{t-1} = l) P(Z_{t-1} = l | Y_0, \dots, Y_{t-1}) \quad (4)$$

161 A NHMM extends this idea by allowing the transition matrix between the hidden states to  
 162 depend on a set of observed covariates  $S_t$ . Hughes and Guttorp [28, 29] highlighted the added value  
 163 of the NHMM to characterize the links between the large-scale atmospheric measures and the  
 164 small-scale spatially discontinuous precipitation field. In the NHMM settings, the transition matrix  
 165 between states  $P(Z_t = k | Z_{t-1} = l)$  in (3) is now time-dependent and conditioned by the covariates  $S_t$ :

166 
$$\pi_{tk} = P(Z_t = k | Y_0, \dots, Y_t, S_t) =$$
  
 167 
$$\frac{1}{K} \sum_{l=1}^K P(Y_t | Z_t = k, S_t) P(Z_t = k | Z_{t-1} = l, S_t) P(Z_{t-1} = l | Y_0, \dots, Y_{t-1}) \quad (5)$$

168 with:

$$P(Z_t=k | Z_{t-1}=l, S_t=PS_t | Z_t=k, Z_{t-1}=l, PZ_t=k | Z_{t-1}=l) /$$

$$k,l | PS_t | Z_t=k, Z_{t-1}=l, PZ_t=k | Z_{t-1}=l \quad (6)$$

The non-homogeneous transition between states is derived from the likelihood of the covariate  $S_t$  given the state transition  $(Z_t, Z_{t+1})$ . We suppose that the probability density function of the covariates during this change of state follows a normal distribution:

$$PS_t | Z_t=k, Z_{t-1}=l = N(\mu_{l,k}, \Sigma_{l,k}) \quad (7)$$

Where  $N$  is a multivariate normal distribution with  $n$  means  $\theta_s = \mu_{l,k}$ ,  $\Sigma_{l,k}$ ,  $\mu$  is here of dimension  $n$ , the number of covariates used to estimate the transitions. For a 'standard' multivariate gaussian distribution  $\Sigma_{l,k}$  is a covariance matrix. In the present application, and to reduce the number of parameters to be estimated, we consider that the predictors are uncorrelated (null covariance) and their relative influence is identical (same variance), i.e.  $\Sigma_{l,k}$  is a multiple of the identity matrix.

181

### 182 **3.1 Estimation of the model parameters**

183

The considered models involve two categories of parameters: those of the observation model,  $\theta_k$ , namely regression coefficient  $B_k$  and standard deviation  $\sigma_k$  for each regime (Eq. 2) and those of the Markov-switching prior, namely  $\theta_s$  (Eq. 5). Given observed  $Y$  and  $X$  series, we proceed to the estimation of model parameters according to a classical maximum likelihood (ML) criterion using an iterative Expectation Maximisation (EM) procedure [30] expressed here without covariates:

$$L(\theta) = \prod_{t=1}^T P(Y_t | Y_{t-1}, \theta) \quad (8)$$

190 where  $\theta = \{\theta_s, \theta_k\}$  is the set of parameters to be estimated. For a given initialization for the  
 191 parameters the EM procedure iterates estimation steps (E-step) of the posterior regime likelihood  
 192  $\pi_k$  with the given modes and the maximisation step (M-step) for the update of the parameters given  
 193 these posteriors. The algorithm iterates until convergence between steps  $n$  and  $n+1$ , i.e.  
 194  $|L\theta(n) - L\theta(n+1)| < 10^{-3}$ . The posterior likelihood  $\pi_k$  (Eq 3&4) of the latent regime  $Z_t$ , is  
 195 estimated in the E-step using the classical forward-backward recursions [31, 32] given series  $X$  and  
 196  $Y$  and current parameter estimate  $\theta_k^{(n)}, \theta_s^{(n)}$ . The M-step re-estimates the parameters  $\theta_k^{(n+1)}, \theta_s^{(n+1)}$ .  
 197 For this, it is often possible to break the optimization problem into several lower dimensional  
 198 optimization problems which are much quicker to solve [32]. More precisely, for all the models  
 199 considered in this paper, it is possible to separate the parameters related to the evolution of the  
 200 hidden Markov chain  $\theta_s$ , and the parameters related to the evolution of the observed process in each  
 201 regime  $\theta_k$ :

$$202 \quad \theta = \underset{\theta_s}{\operatorname{argmax}} \sum_{t=0}^T \log(P(Z_t=k | Z_{t-1}=l, S_t, \theta_s(n)) P_{Z_t=k, Z_{t-1}=l} | Y_0.. Y_T, S_t, \theta(n)) \quad (9)$$

$$203 \quad \theta_k = \underset{\theta_k}{\operatorname{argmin}} \sum_{t=0}^T P_{Z_t=k} | Y_0.. Y_T, \theta(n) (Y_t - B_k X_t)^2 \quad (10) \quad \sigma_k(n+1) = \sum_{t=0}^T P_{Z_t=k} | Y_0..$$

$$204 \quad \sum_{t=0}^T P_{Z_t=k} | Y_0.. Y_T, \theta(n) (Y_t - B_k X_t)^2 \quad (11)$$

205

### 206 **3.2 Forecasting application**

207

208 The considered multi-regime regression models are applied to the short-term forecasting of  
 209 series  $Y$ . More precisely, at a given time  $t$ , we aim at predicting variable  $Y$  at time  $t+dt$ . We  
 210 typically assume that prediction variables  $X$  and covariates  $S$ , typically numerical simulations, are  
 211 available up to time  $t+dt$  whereas the variable  $Y$  is only known up to time  $t$ .  $\theta$  is estimated using  
 212  $X_{0..t+dt}$  and  $S_{0..t+dt}$  (for inhomogeneous transitions). Thus,  $Y_{t+dt}$  is given by the conditional

213 expectation of variable  $Y_{t+dt}$  given observations series up to time  $t$  and predictor series up to time  $t+$   
214  $dt$ :

215 
$$(12)$$

216 For HMM and NHMM it resorts to:

217 
$$(13)$$

218 For autoregressive models HMM-AR and NHMM-AR, i.e.  $X_{t+dt}$  contains  $Y_{t+dt-1}$  which is not  
219 available, is estimated using  $Y_{t...}$ ,  $X_{t..}$ ,  $X_{t+dt-1}$  and . Estimated  $Y_{t+dt}$  resorts to:

220 
$$(14)$$

221 It might be noted that these predictions actually account for the uncertainties in the  
222 determination of the underlying regimes. Contrary to deterministic methods, confidence interval  
223 and uncertainties on  $Y_{t+dt}$  can be derived [33] which is a key issue for modeling considerations.

224

### 225 **3.3 Model performance estimation**

226

227 A key issue in practice, which has received lots of attention in the last few years, is the problem  
228 of model selection which aims at finding the "optimal" number of predictors and covariates [31].  
229 Hereafter, we have chosen to use both the Bayes Information Criterion (BIC) and the explained  
230 variance (EVAR) as a first guides. BIC index generally permits to select parsimonious models  
231 which fit the data well [34]. It is defined as:

232 
$$\text{BIC} = -2 \log^*(L) + p^* \log(S) \quad (15)$$

233 Where L is the likelihood of the data, p is the number of parameters and S is the number of  
234 observations. The likelihood which is an output of the backward-forward recursions performed in  
235 the E-step. We also use the classical explained variance, EVAR, to characterize the model  
236 relevance:

$$237 \quad \text{EVAR} = 1 - \frac{\text{var}(Y_{t+1} - \hat{Y}_{t+1})}{\text{var}(Y_{t+1})} \quad (16)$$

238 BIC and EVAR are partially linked [34]. BIC tends to penalize complex models whereas  
239 explained variance criterion only qualifies the result and may lead to the over-parameterization of a  
240 model that typically lead to errors when other dataset are tested using the same parameterization.  
241 Therefore we consider both BIC and EVAR to assess the model performance.

242 The choice of the predictors and the covariates is performed here as follows. We first select as  
243 predictors the variable showing a significant correlation with the studied variable. Given these  
244 predictor datasets, we tested all the possible configurations and chose the predictors which provide  
245 the lower BIC on the training dataset and the greatest EVAR using the training (EVAR\_train) and  
246 the validation dataset (EVAR\_valid).

247

## 248 **4 The data**

249

### 250 **4.1 The studied variable**

251

252 Non-algal SPM concentrations (SPIM) are estimated using an analytical algorithm [12] defined  
253 as the difference between total SPM and phytoplankton biomass, the latter derived from Chl-a. It  
254 incorporates mainly mineral SPM and smaller amounts of organic SPM not related to living

255 phytoplankton. This method to derive non-algal SPM from remote-sensing reflectance is based on  
256 the inversion of a simplified equation of radiative transfer, assuming that chlorophyll concentration  
257 is known. This merged dataset consists of fields of non-algal surface SPM concentrations, derived  
258 from the Sea-viewing Wide Field-of-view Sensor (SeaWiFS), the Moderate Resolution Imaging  
259 Spectroradiometer (MODIS) and the Medium Resolution Imaging Spectrometer (MERIS) sensors,  
260 provided by the Ocean Colour TAC (Thematic Application Facility) of MyOcean, and interpolated  
261 with a kriging method [35] for the period 2007–2009 over the Gironde mouth river from 3°W-1°E ;  
262 45-46.5°N. Finally 5682 continuous time series of 1096 days compose our initial dataset of mineral  
263 suspended matters concentration.

264 We first account for the space-time variability of the dataset, previously detrended and centered  
265 for each time series [37] using a EOF decomposition [21], expressed here using the matrix form:

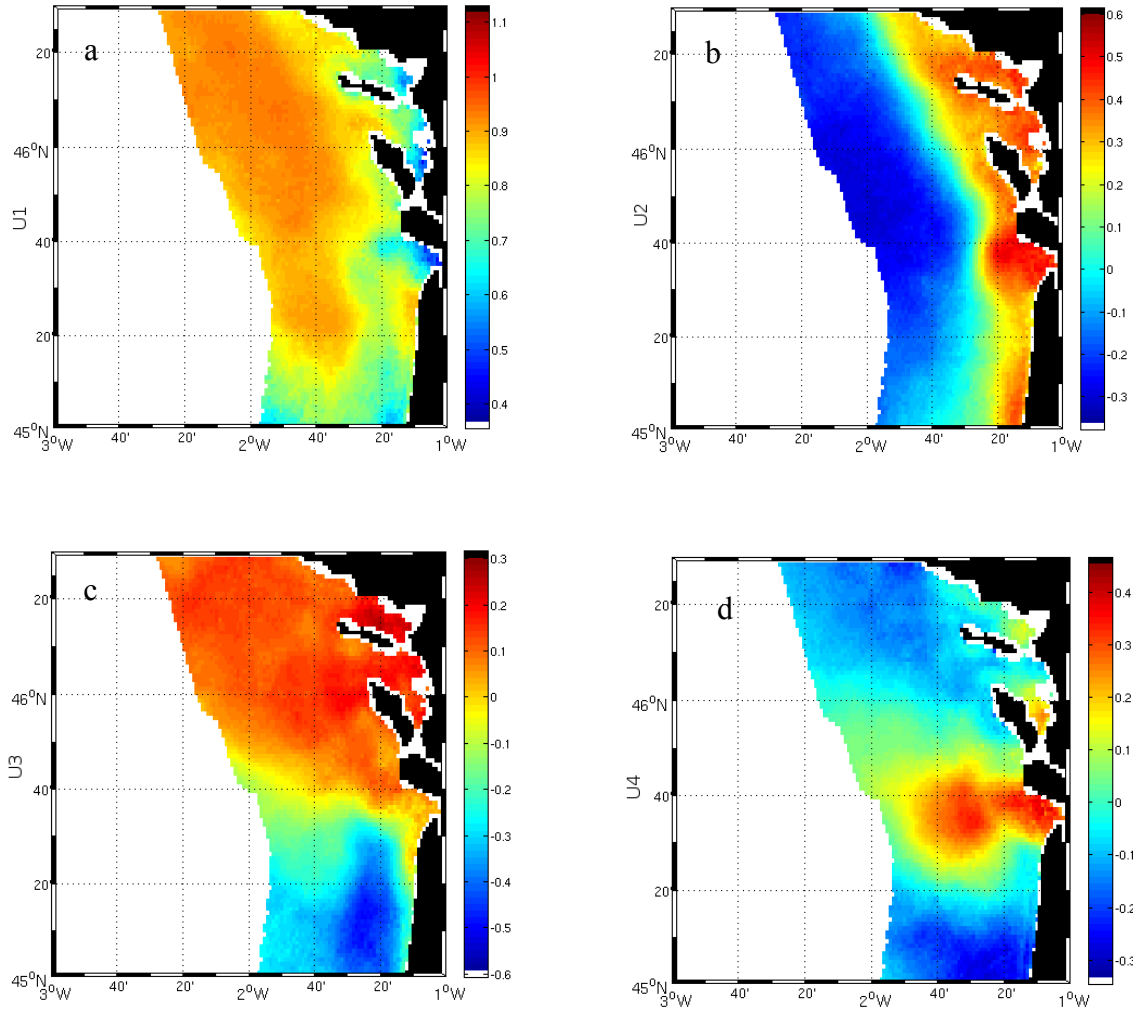
$$266 \quad \text{Cov}(\text{SPIM}) = \text{UVU}^t \quad (17)$$

267 where U is a here 5682\*5682 matrix containing the spatial modes (Eigenvectors) of the  
268 covariance decomposition (ordered by percentage of explained variance). Associated with each  
269 spatial mode k, its expansion coefficient (also referred in the literature as principal component) is  
270 the time evolution of the k<sup>th</sup> mode:

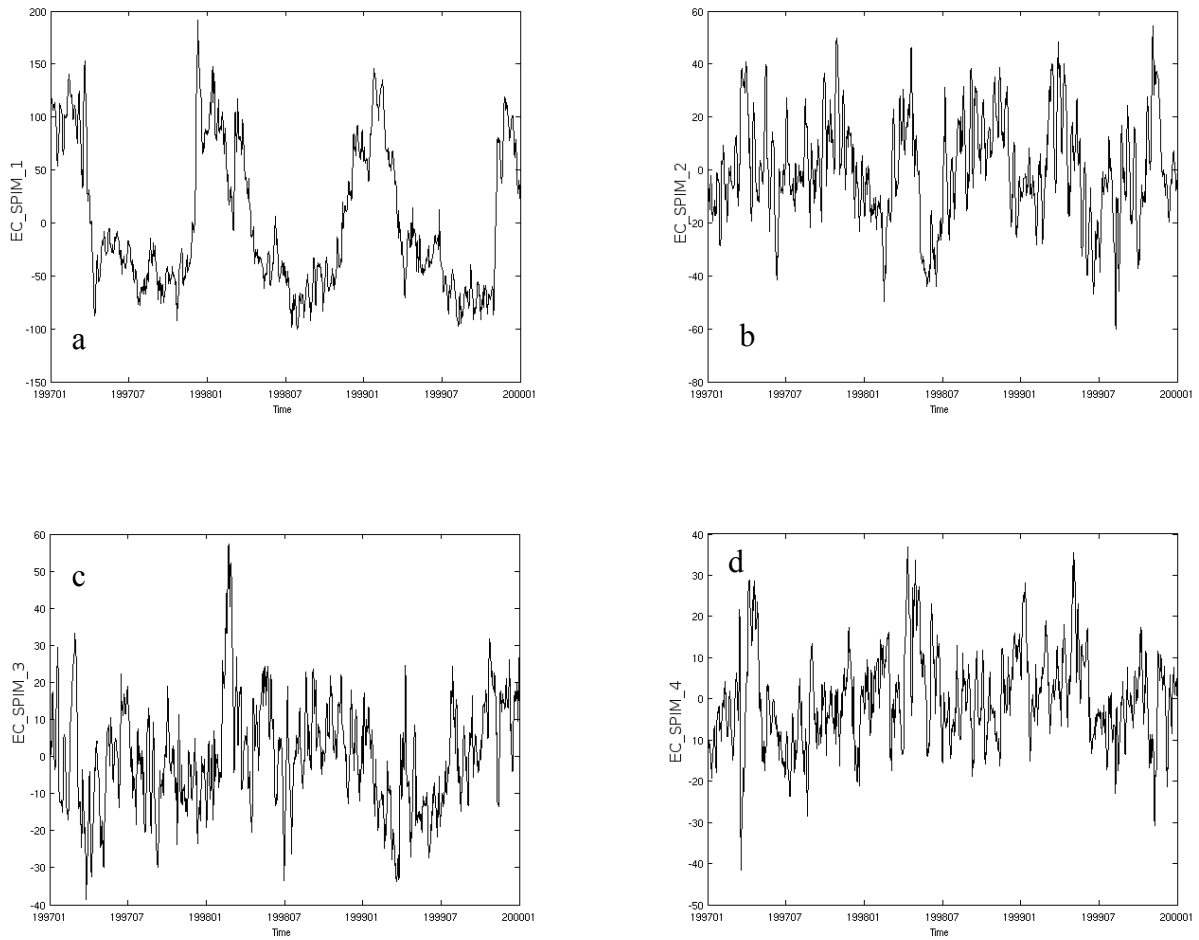
$$271 \quad \text{EC\_SPIM}_{k,t} = \text{SPIM}_t * U_k \quad (18)$$

272 Figure 2 shows the four first spatial modes of the EOF decomposition. Figure 3 depicts the four  
273 associated time series  $\text{EC\_SPIM}_{i=1,4}$ . The first mode (Fig.2a) comprises 85% of the total variance. It  
274 clearly addresses the seasonal cycle as shown in Fig. 3a where the switch between winter (high  
275 values of  $\text{EC\_SPIM}_1$  correspond here to high values of SPIM observed in winter) and summer  
276 periods is clearly visible. The variability around the seasonal mean is captured by the other modes  
277 (Fig.2 c-e & Fig 3 c-e). Mode 2 refers to the inter-annual and the intra-seasonal variability in the  
278 shoreward gradient and represents 7% of the total variance. Mode 3 addresses some North-South

279 gradients and represents 4% of the total variance and mode 4 is clearly influenced by the Gironde  
280 river (Fig. 2d), which brings sediments during water outflow, and represent 3% of the variance. By  
281 construction, EOF decomposition imposes the orthogonality [21] of the spatial modes (Fig. 2).



282 Figure 2: spatial modes of the EOF decomposition of the SPIM observed from satellite from  
283 2007-2009 in the Gironde mouth river. From left to right and top to bottom the first four EOF  
284 modes account respectively for 85, 7, 4 and 3% of the total variance.

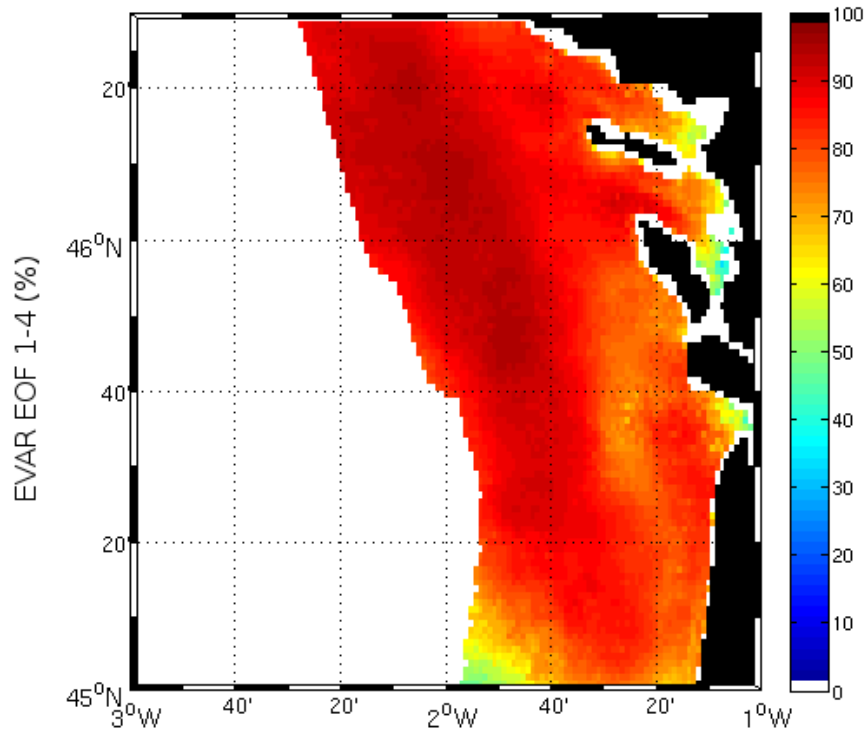


285 **Figure 3:** EOF decomposition of the SPIM observed from satellite from 2007-2009 in the  
 286 Gironde mouth river: from left to right and top to bottom, the expansion coefficients (EC\_SPIM<sub>1-4</sub>)  
 287 associated with the first four EOF modes depicted in Fig. 2, i.e. the time evolution of the spatial  
 288 modes. The reconstruction of the SPIM variable from the estimated ECs is performed as:

289 
$$SPIM_t = k EC\_SPIM . Uk \quad (19)$$

290 The total explained variance using the 4 first modes is shown Fig. 4. On average, the explained  
 291 variance represents 99 % of the total variability on the areas with some local minima of 60%  
 292 observed at the very near-shore and the Southwestern part of the area.





293

294 Figure 4: Variance explained by the four first modes of the EOF decomposition of the  
 295 suspended matters.

296

## 297 **4.2 Predictors and covariates**

298

299 The predictors X are the variables used in the estimation of Y and Z any time (Eq. 13 & 14). We  
 300 used here wave height (WH) daily means of the Wave Watch 3 model (WW3; [24, 36]) provided by  
 301 the IOWAGA and PREVIMER programs, Western and Northern winds interpolated from  
 302 QuickSCAT and ASCAT observations in conjunction with ECMWF forecasting [25], provided by  
 303 Ifremer, tide index (SHOM, 2000) at Bordeaux and the flow measurement of river la Gironde.  
 304 Similarly to the SPIM data, all the data were log transformed. For the wind data which is signed, the  
 305 transformed log variable was signed negatively a posteriori to the log transformation. The WH first  
 306 mode of the EOF decomposition explained 98 % of the total variance, 93% for the Northern wind

307 (WND1), and 96% for the Western wind (WND2). Covariates are the normalized predictors used in  
308 the estimation but considered at  $t-2$ . This lag has been estimated as the optimal time-lag using BIC  
309 and EVAR results on the training dataset.

310

## 311 **5 Results**

312

313 We summarize in Table 1 the prediction performance for the first four ECs of the SPIM issued  
314 from four models: HMM, NHMM, HMM-AR, and NHMM-AR. The number of considered modes  
315 for the mixture varies from 1 to 3. The one-mode models refer to a simple multivariate regression  
316 analysis. For each configuration we provide the BIC and EVAR\_train on the training dataset  
317 (2007-2009) and EVAR\_valid on the validation dataset (2010). Note that the selection of the  
318 predictors and resulting covariates is achieved as a prior step as described in Section 2.6. The first  
319 mode of the EOF decomposition explains 85% of the total variance. EC\_WH<sub>1</sub> and EC\_WND2<sub>1</sub>  
320 (respectively the expansion coefficient of the first EOF of the Western winds) are identified as  
321 being the relevant predictors. This mode captures the mean seasonal variability of the SPIM, which  
322 is mainly driven by WH and the North Atlantic storms and at a second order by the Western winds.  
323 For EC\_SPIM<sub>1</sub>, when no autocorrelation term is used, the best fit is obtained for a 3-regime  
324 NHMM model (BIC= 9873, EVAR\_train=90% and EVAR\_valid=85%). When a first order  
325 autocorrelation term is added, the best fit is issued from a 3-regime HMM-AR model: BIC= 7997,  
326 EVAR\_train = 98% and EVAR\_valid = 97%. The lag-1 autocorrelation value is 0.85 for  
327 EC\_SPIM<sub>1</sub>, and therefore the weight given  $Y_{t-1}$  is important compared to the other covariates,  
328 EC\_WH<sub>1</sub> and EC\_WND2<sub>1</sub>. This stresses the fact that when available first autoregressive term  
329 should be included to enhance the performances

pas  
clair

330 The second mode of the EOF decomposition of the SPIM variability explains 7% of the total  
 331 variance. The selected predictors are the first mode of the Western wind, the tide, and the river  
 332 flow. The variability captured by EC\_SPIM<sub>2</sub> relates to the local Westward wind, which is not  
 333 captured by the **WH** model, and the very coastal variability introduced by the tide and the river  
 334 outflow. For the non-AR models the selected model was the three-regime NHMM. It is interesting  
 335 to note in this case that EVAR<sub>valid</sub> increased from 50 to 73% between the HMM and the NHMM,  
 336 highlighting the contribution of the non-homogeneous transition model. By contrast, the HMM-AR  
 337 performed slightly better than the NHMM-AR. niveau de contribution des variables complémentaires

338 Table 1: Model performance for each EOF mode of the SPIM variability. For each  
 339 configuration we report the BIC (a) and the explained variance (EVAR<sub>train</sub>, b) for the training  
 340 dataset (2007-2009), and the explained variance (EVAR<sub>valid</sub>, c) for the validation dataset (2010).  
 341 In bold are highlighted for each EC the selected configurations (see § 5.2).

EC_SPIM	Number of modes, M					
	1	2	3	1	2	3
1	HMM (a) 11183 (b) 37 (c) 32	HMM 10037 84 70	HMM 9874 85 75	HMM-AR 8157 92 91	HMM-AR 7986 95 93	HMM-AR <b>7997</b> <b>98</b> <b>97</b>
	NHMM 11184 37 34	NHMM 10037 84 71	NHMM <b>9873</b> <b>90</b> <b>85</b>	NHMM-AR 8171 92 90	NHMM-AR 7994 92 94	<b>NHMM-AR</b> 8018 98 97
2	HMM 9403 18 12	HMM 8579 67 33	<b>HMM</b> 8129 76 50	HMM-AR 7167 90 87	HMM-AR 7098 91 89	HMM-AR <b>7075</b> <b>92</b> <b>91</b>
	NHMM 9451 18 12	NHMM 8614 67 44	NHMM <b>8152</b> <b>79</b> <b>73</b>	NHMM-AR 7188 89 88	NHMM-AR 7383 90 87	NHMM-AR 7070 92 90
3	HMM 8840 12 7	HMM 8222 57 44	<b>HMM</b> 7844 68 72	HMM-AR 6723 85 84	HMM-AR 6632 86 91	HMM-AR <b>6630</b> <b>88</b> <b>92</b>

	NHMM 8866 11 16	NHMM 8246 59 45	NHMM <b>7862</b> <b>75</b> <b>76</b>	NHMM-AR 6745 88 86	NHMM-AR 6673 88 91	NHMM-AR 6703 88 92
4	HMM 8248 18 28	HMM 7596 60 63	HMM 7285 71 72	HMM -AR 6398 85 86	HMM -AR 6416 85 86	HMM -AR <b>6313</b> <b>86</b> <b>86</b>
	NHMM 8276 18 28	NHMM 7628 62 59	NHMM <b>7267</b> <b>70</b> <b>75</b>	NHMM-AR 6426 85 83	NHMM-AR 6445 85 83	NHMM-AR 6357 86 85

342

343 The third mode of the EOF decomposition of the SPIM variability explains 4% of the total  
344 variance. It captures some inter-annual and intra-seasonal variability of the latitudinal gradient of  
345 the SPIM. The selected predictors are EC\_WH<sub>1</sub>, EC\_WND1<sub>1</sub> (Northern) and the tide. Once again,  
346 three-regime NHMM and HMM-AR provide the best results.

347 Regarding the fourth mode of the EOF decomposition of the SPIM variability, which accounts  
348 3% of the total variance, EC\_WH<sub>1</sub>, EC\_WND2<sub>1</sub>, the tide and the river flow are selected as  
349 contributive predictors. We reconstruct 75 % of EC\_SPIM<sub>3</sub> variance of the validation dataset using  
350 a three-regime NHMM and 86% using a three-regime HMM-AR. We note that globally, the three  
351 indices (BIC, EVAR\_train and EVAR\_valid) tend to select the same models.

352

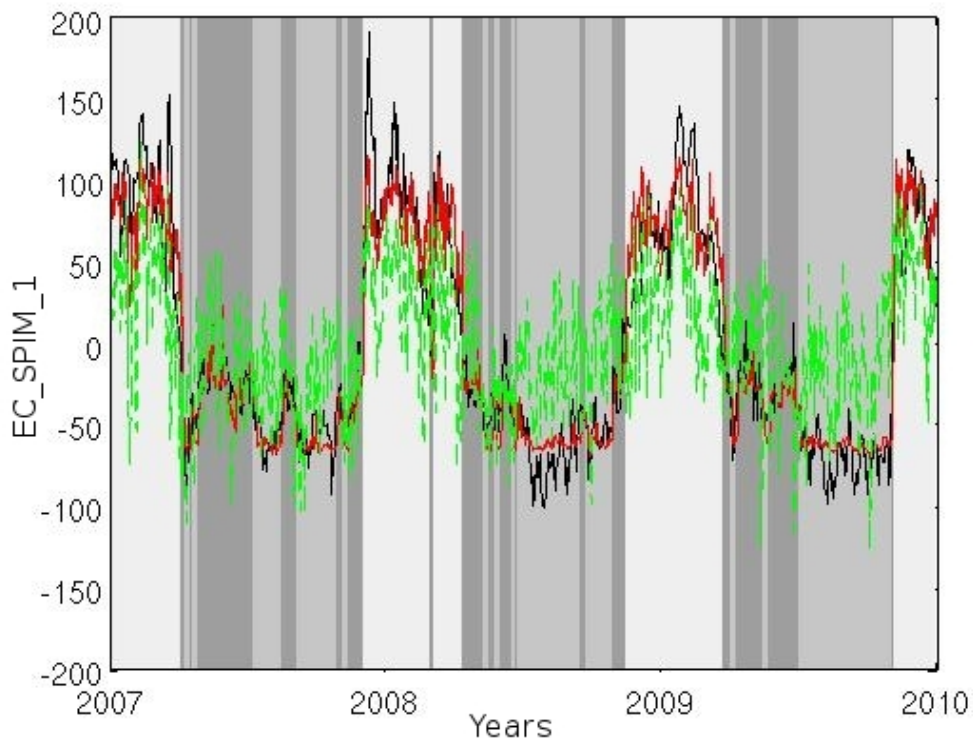
### 353 **5.1 Example with the estimation of EC\_SPIM<sub>1</sub>**

354

355 We report in Figure 5 the temporal evolution of the three regimes of the NHMM for EC\_SPIM<sub>1</sub>.  
356 In table 2 are shown the corresponding coefficients for each predictor and the intercept. The first  
357 regime (light grey), characterized by high SPIM levels (intercept of 65), is referred as a ‘winter  
358 regime’. The ‘winter regime’ also strongly relates to the wave height (WH regression coefficient of  
359 0.6). Dark grey periods (regime 3) are identified as a ‘transition regime’, and medium grey (regime

360 2) identified as the ‘summer regime’. For regimes 2 and 3, the coefficients for WH decrease  
361 respectively to 0.12 and 0.09. In summer the energy brought by waves is not sufficient enough to  
362 re-suspend massively the sediments. It might be noticed that for all regimes the wind conditions  
363 show a small but significant effect on  $EC\_SPIM_1$ . When an autocorrelation term is added (HMM-  
364 AR, table 2), the AR(1) coefficient value is 0.86 for the regime 1 (winter), and 0.9 for regime 2 and  
365 3 which underlies the natural higher autocorrelation level of SPIM when the concentration is low.

366 Figure 4 compares the prediction of  $EC\_SPIM_1$  using a single multivariate regression (green)  
367 and the proposed multi-regime NHMM. In this case the explained variance value (Table 1) is of  
368 37% for the multivariate regression model compared to 85% for the three-regime NHMM.



369

370 Figure 5: Estimation of the  $EC\_SPIM_1$  (in black) using  $EC\_WH_1$ ,  $EC\_WND2_1$  and a single  
371 regression (green) and a 3 regime NHMM (red). The nuances of grey in the background highlight  
372 the temporal distribution of the regimes.

373

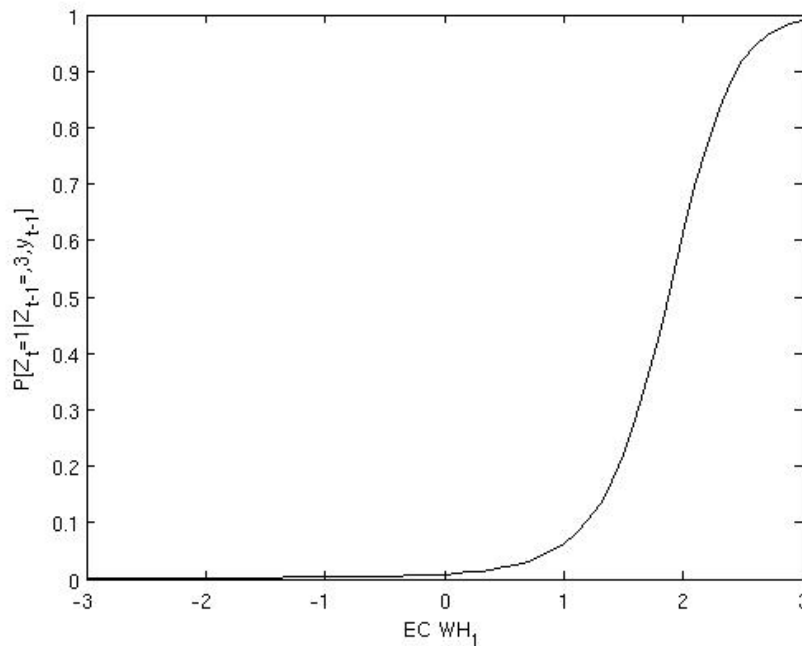
374 Table 2: Estimated regression parameters for each of the three regimes of the NHMM and the  
 375 HMM-AR for the first mode of the SPIM EOF decomposition: regression parameters involve an  
 376 intercept and the regression coefficients of the wave height and western wind velocity.

	EC_WH <sub>1</sub>	EC_WND <sub>2</sub>	Intercept	
NHMM	(1, winter) 0.6037	-0.0632	65.0672	
	(2, summer ) 0.0910	0.0006	-61.6442	
	(3, transition) 0.1210	0.0100	-24.6578	
	EC_WH <sub>1</sub>	EC_WND <sub>2</sub>	Intercept	AR(1)
HMM-AR	(1) 0.2383	-0.0033	4.4694	0.86
	(2) -0.0050	0.0168	-3.9531	0.90
	(3) 0.0354	0.0035	0.6079	0.90

variance  
expliqué par  
chaque  
terme

377

378 Figure 6 illustrates the non-homogeneous transition used in the NHMM between the ‘transition’  
 379 ( $Z_t=3$ ) and ‘winter’ ( $Z_t=1$ ) regimes. The probability of switching from regime 3 to 1 increases with  
 380 wave height covariate  $WH_1$  with a probability of switching close to zero when  $WH_1$  is negative and  
 381 a probability close to one for large  $WH_1$  values.



382

383 Figure 6: Non-homogeneous transition between ‘transition regime’ ( $Z_t=3$ ) (light grey Fig. 5)  
 384 and ‘winter regime’ ( $Z_t=1$ ) (light grey Fig. 5) as a function of the wave height covariate  $WH_1$ .

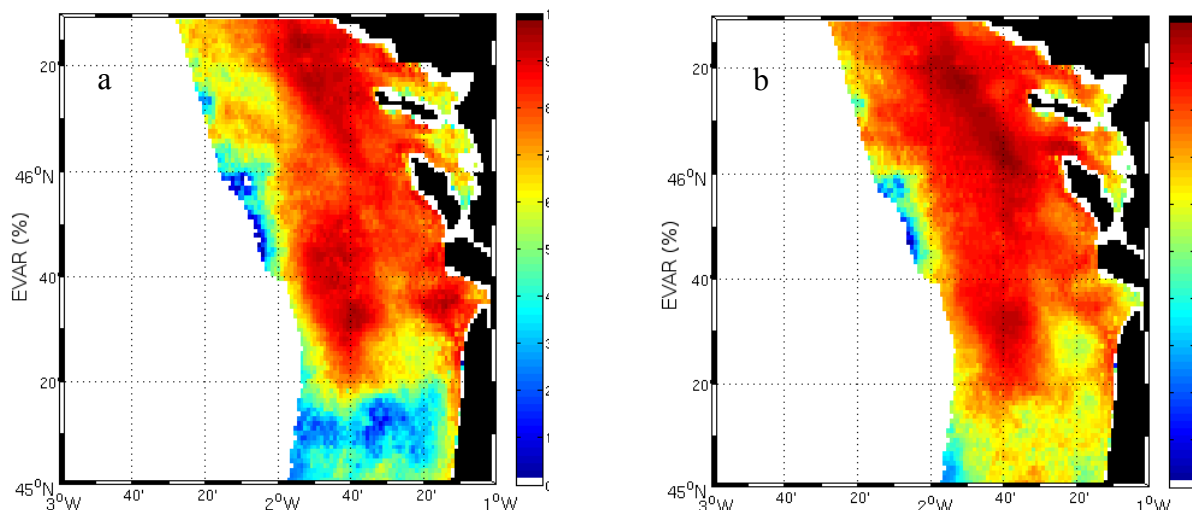
## 385 **5.2 Forecasting of the SPIM on the 2010 validation dataset**

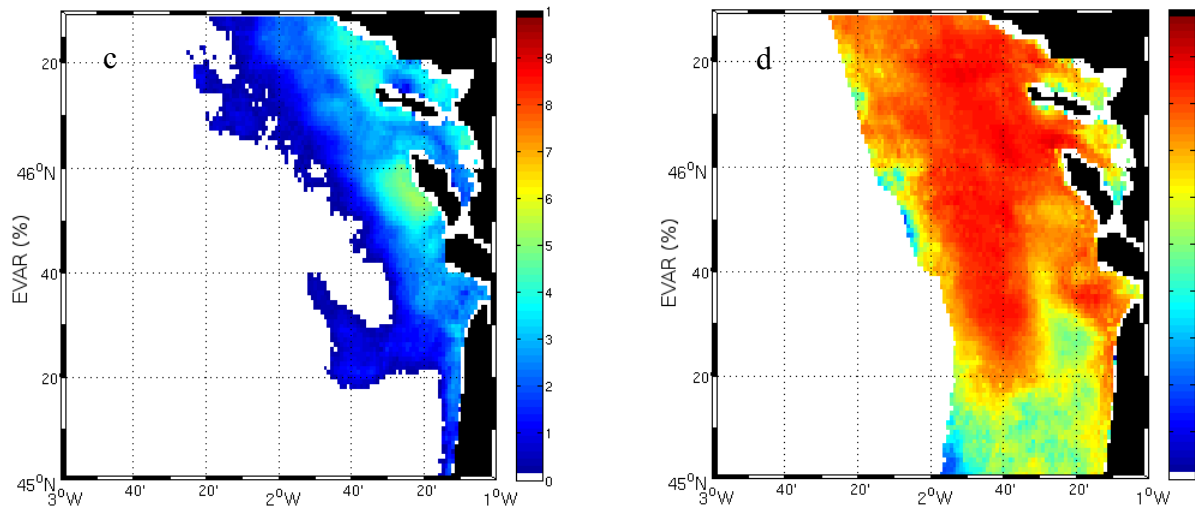
386

387 We forecast SPIM fields from the reconstructed ECs and the selected models (Table 1 & Eq.  
388 19). Figure 7a&7b compare **EVAR\_valid** of the initial field (SPIM) using the three-regime NHMM  
389 and NHMM-AR models selected in Table 1 for their results. On average we were able to predict at  
390  $t+1$  80% of the variance using the NHMM (Fig. 7a) and 90% using the NHMM-AR. **The spatial**  
391 **distribution of the error is not homogeneous.** Fig. 7a shows that **EVAR\_valid** value is of 90% in the  
392 **Northern part with nevertheless poorer results in the South.** Fig. 7b shows that the  $AR_1$  component  
393 **of the model increases EVAR for the whole area.**

394 **We also consider the results of a standard multi-regression analysis.** If only one regime is  
395 **considered NHMM and HMM resort to a standard multivariate regression and NHMM-AR and**  
396 **HMM-AR to a standard multivariate regression including an  $AR_1$  coefficient the transition**  
397 **probabilities being equal to 1.** Fig. 7c shows the obtained results with the standard multivariate  
398 **regression and Fig 7d the standard multivariate regression including an  $AR_1$ .** From Fig. 7c to 7a, the  
399 **gain in explained variance is in mean about 250% (from in mean 32% Fig. 7c to 80% Fig. 7a) while**  
400 **for the AR models, the gain is about from 11% (from in mean 83% Fig. 7d to 93% Fig. 7b).**

401





402 Figure 7: Explained variance for the 2010 validation dataset reconstructed using the selected 3-  
 403 regime NHMM (a) and NHMM-AR (b), compared with the standard multivariate regression  
 404 without  $AR_1$  (c) and including an  $AR_1$  (d).

405 To consider the model forecast performances, we report the short-term forecast results at  
 406 different time steps (cf. Eq.13 & 14). For the HMM-AR and NHMM-AR (Eq. 14) is the estimated  
 407 value, the observation being not available (see § 3.2). Table 3 synthesizes the explained variance  
 408 statistics using 3 regimes and the four tested models for the forecasting at t+1, t+5 and t+15 and the  
 409 validation 2010 dataset (Eq. 19).

410 The long term forecasting results are globally better with the NHMM. At t+15 using the  
 411 NHMM we are able to forecast 74% of the variance for 2010, compared with 40% for the HMM. In  
 412 this case where the covariates and predictors (mode outputs for which the short term predictions are  
 413 assumed to be available) are used in the estimation of the regime transition probability . For  
 414 autoregressive models, at t+15, we were able to forecast 75% of the 2010 variance with the  
 415 NHMM-AR compared with 70% with the HMM-AR. For the NHMM-AR the covariates help in the  
 416 estimation of both and . At t+15 NHMM and NHMM-AR show equivalent results underlying the  
 417 maximal time-step to consider for the between these two models.



418 Table 3: Validation results on year 2010. Explained variance (Eq. 16) for the forecast at t+1, t+5  
 419 and t+15 of the 2010 validation dataset.

EVAR for the 2010 validation dataset	
HMM (t+1) 73 (t+5) 63 (t+15) 40	HMM-AR 93 80 70
NHMM (t+1) 80 (t+5) 77 (t+15) 74	NHMM-AR 93 82 75

420

421 SVR model was also evaluated to evaluate the performances of a non-linear model on the studied  
 422 dataset. To perform the comparison, we train the SVR model (<http://www.csie.ntu.edu.tw>) for each  
 423 EC using the same training dataset (2007-2009) and performed forecasting using the same  
 424 validation dataset (2010). We used the setting as following: model epsilon-SVR ( $s=3$ ), linear or  
 425 polynomial kernel ( $t=0$  or 1) and the same inputs (predictors, covariables) for each EC. Parameters  
 426  $c$  and  $g$  [10] were optimised for each EC using the training dataset and the cross validation mode.  
 427 On the 2010 validation dataset, better forecast results reached 40% at t+1 of the EVAR (without  
 428 AR) and 85% with an AR coefficient. The results were significantly worse than those obtained  
 429 using the time-varying models for increasing time steps. The SVR can address non-linear  
 430 relationships, it cannot nevertheless deal with multi-regime processes. By contrast, the latent-regime  
 431 model addresses by nature multi-regime processes and can approximate non-linear relationships as  
 432 a series of linear models.

433

## 434 **6 Discussion**

435

436 We investigated the relevance of four regime-switching latent regression models, namely  
437 HMM, NHMM, HMM-AR and NHMM-AR to characterize time-varying linear relationships  
438 between the high resolution inorganic suspended matter concentration (SPIM), estimated from 2007  
439 to 2009 using MODIS, SeaWiFS and MERIS data in a coastal area, and its forcing conditions, i.e.  
440 the wave height, the Northern and Western winds, the tides and the river flow. The estimated  
441 regimes are then used to forecast the SPIM using the independent year 2010 dataset, from  $t+1$  to  
442  $t+15$ .

443 An optimal number of three distinct geophysical regimes were needed to capture the different  
444 dynamics and optimize forecasting performance. Autoregressive and non-homogeneous model  
445 showed better performances. With the evaluated models and the 2010 validation dataset we were  
446 able to forecast at  $t+1$  80 % of the variance explained using a NHMM and 93 % using a NHMM-  
447 AR. In the latest case the strong natural autocorrelation of the studied signal is an important  
448 predictor to consider. The explained variance on the prediction at  $+1$  for a standard multivariate  
449 regression was of 32% and 80% (with an  $AR_1$  term). Using a SVR we were able to forecast at  $t+1$   
450 respectively 40% and 85% (with an  $AR_1$ ) of the explained variance.

451 As illustrated for the first SPIM EOF component (Figure 5), the proposed multi-regime setting  
452 allowed us to identify three seasonally varying relationships between the observed turbidity, the  
453 wave height and the wind. We did not drive the model to account for seasonal regimes but we  
454 identified three seasonally-discriminated regimes, with two leading factors: the mean SPIM level  
455 (intercept) and the Western wave height. These regimes identified directly physical behaviors, here  
456 the minimum of energy to be brought by the Western swell to re-suspend the sediments. This is  
457 regarded as a key feature of the latent-regime model compared to other non-linear regression  
458 models, such as Neural Networks [38] or SVR [10] which cannot address multi-regime

459 relationships and are hardly interpreted in general. Using our dataset the non-linear SVR was not  
460 able to retrieve the regime changes.

461 Regarding long-term forecast performance, at t+15 best results obtained were of 74% of  
462 explained variance for the NHMM and 75% for the NHMM-AR. For short period, typically from 1  
463 to 15 days, when the observed Y is not available, NHMM-AR provided the best results. In this case  
464 the predictors and covariates are used in the estimation of both and . At t+15 NHMM and NHMM-  
465 AR showed similar results underlying the maximal time-step to consider, when no observation of Y  
466 is available, for the choice between these two models.

467 In the future, we will address the forecasting of the chlorophyll-a using satellite-derived  
468 observations such as the photosynthetic available radiation, the temperature, the suspended matters  
469 (as index of available nutrients) and light attenuation [39]. In this more complicated case, second  
470 order relationships between the variable and its predictors have to be evaluated, the chlorophyll-a  
471 dynamic being not anymore a passive result of the forcing conditions, as expected with the SPIM,  
472 but having its proper characteristics depending on each phytoplankton specie. Extensions of the  
473 considered latent regime setting to other inverse problems in satellite sensing data analysis are also  
474 under investigation, such as latent regime inversion procedures for satellite-derived chlorophyll-a  
475 concentration to account for different water types (turbid or not turbid) and/or the presence of  
476 specific phytoplankton species.

## 477 **7 Acknowledgements**

478

479 The authors thank Aldo Sottolichio from the Université of Bordeaux 1, for the provision of the  
480 in-situ Gironde flow measurement, Pierre Tandeo for fruitful advises and the MCGS (Marine  
481 Collaborative Ground Segment; <http://www.mcgs.fr>) project which aim at making the most of ESA  
482 Sentinels satellites potential for users driven services based on high level products. MCGS

483 addresses the need of the European Space Agency to build up data processing centers in  
484 conjunction with the Copernicus Program for the provision of services to local and national, public  
485 and private European institutions or entities involved in marine activities. The project is co-funded  
486 by the French Government (Fonds Unique Inter-ministériel), local authorities of the Bretagne and  
487 Provence-Alpes-Côte d'Azur regions and the European Regional Development Fund (ERDF), under  
488 support of the French Space Agency (CNES).

## 489 **8 References**

490

491 1 P. Lazure, V. Garnier, F. Dumas, C. Herry, M. Chifflet. “Development of a hydrodynamic model of  
492 the Bay of Biscay”. Validation of hydrology. *Continental Shelf Research*, 29(8), 985-997, 2009.

493 2 L. Debreu, P. Marchesiello, P. Penven and G. Cambon, “Two-way nesting in split-explicit ocean  
494 models: algorithms, implementation and validation”, *Ocean Model.*, 49-50, 1-21, 2012.

495 3 A. Sottolichio, P. Le Hir, P. Castaing. “Modeling mechanisms for the turbidity maximum stability in  
496 the Gironde estuary, France”, *Coastal and Estuarine Fine Sediment Processes*, pp 373-386, 2000.

497 4 A. Rivier, F. Gohin, P. Bryere, C. Petus, N. Guillou, G. Chapalain. “Observed vs. predicted  
498 variability in non-algal suspended particulate matter concentration in the English Channel in relation to tides  
499 and waves”. *Geomarine Letters*, 32(2), 139-151, 2012.

500 5 C. Aitken, “On Least Squares and Linear Combinations of Observations”, *Proceedings of the Royal*  
501 *Society of Edinburgh*, 55, 42–48, 1935.

502 6 William E. Wecker, Craig F. Ansley, *The Signal Extraction Approach to Nonlinear Regression and*  
503 *Spline Smoothing Journal of The American Statistical Association* , 78(381):81-89, 1983.

504 7 Box, George; Jenkins, Gwilym, *Time Series Analysis: forecasting and control*, rev. ed., Oakland,  
505 California: Holden-Day, 1976.

- 506 8 Tesfaye, Y. G., Meerschaert, M. M., and Anderson, P. L. Identification of periodic autoregressive  
507 moving average models and their application to the modeling of river flows. *Water Resources Research*,  
508 42(1), 2006
- 509 9 Some Neural Network applications in environmental sciences part I: forward and inverse problems in  
510 geophysical remote measurements, V. Krasnopolsky and H. Schiller, *Neural Networks*, vol 16 (2003), 321-  
511 334.
- 512 10 Chih-Chung C., Chih-Jen L. LIBSVM: A library for support vector machines *Transactions on*  
513 *Intelligent Systems and Technology (TIST)*, 2011.
- 514 11 P. Ailliot, V. Monbet. “Markov-switching autoregressive models for wind time series”.  
515 *Environmental Modelling & Software*, 30, 92-101, 2012.
- 516 12 F. Gohin, S. Loyer, M. Lunven, C. Labry, J.M. Froidefond, D. Delmas, M. Huret, A. Herbland,  
517 “Satellite-derived parameters for biological modelling in coastal waters: illustration over the eastern  
518 continental shelf of the Bay of Biscay”. *Remote Sensing of Environnement* 95(1), 29–46, 2005.
- 519 13 D. Doxaran, « Télédétection et modélisation numérique des flux sédimentaires dans l’estuaire de la  
520 Gironde », PhD thesis, University Bordeaux 1, France, 326 pp, 2002.
- 521 14 D. Doxaran, J.M. Froidefond, P. Castaing and M. Babin. “Dynamics of the turbidity maximum zone  
522 in a macrotidal estuary (the Gironde, France): Observations from field and MODIS satellite data”, *Estuarine*  
523 *Coastal and Shelf Science*, 81, 321–332, 2009.
- 524 15 D.G. Bowers, C.E. Binding.”The optical properties of mineral suspended particles: a review and  
525 synthesis”. *Estuarine Coastal Shelf Science*, 67(1/2), 219–230, 2006.
- 526 16 D. Eisma, P. Bernhard, G.C. Cadée, V. Ittekkot, J. Kalf, R. Laane, J.M. Martin, W.G. Mook, A. Van  
527 Put, T. Schuhmacher, “Suspended matter particle size in some West-European estuaries; part II: a review on  
528 flocculation and break up”, *Netherlands Journal of Sea Research*, 28(3), 215–220, 1991.
- 529 17 W. S. DeSarbo and W. L. Cron, “A maximum likelihood methodology for clusterwise linear  
530 regression”, *Journal of Classification*, 5, 249–282, 1998

531 18 P. Tandeo, B. Chapron, S. Ba, E. Autret, R. Fablet, “Segmentation of Mesoscale Ocean Surface  
532 Dynamics Using Satellite SST and SSH Observations Geoscience and Remote Sensing”, IEEE Transactions  
533 on Volume, pp 1 – 9, 2013.

534 19 B.H. Juang, and L.R. Rabiner. “Hidden Markov models for speech recognition”, *Technometrics*, 33,  
535 251-272, 1991.

536 20 C. Frankignoul and K. Hasselmann, “Stochastic climate models. Part II: Application to SST  
537 anomalies and thermocline variability”. *Tellus*, 29, 289-305, 1977.

538 21 R.W. Preisendorfer, “Principal Component Analysis in Meteorology and Oceanography”, Elsevier,  
539 New York, pp 425, 1988.

540 22 Cressie NAC, Wikle CK. *Statistics for Spatio-Temporal Data*. Wiley; New York: 2011.

541 23 Abdi, H. "Discriminant correspondence analysis." In: N.J. Salkind (Ed.): *Encyclopedia of*  
542 *Measurement and Statistic*. Thousand Oaks (CA): Sage. pp. 270–275, 2007.

543 24 F. Ardhuin, E. Rogers, A.V. Babanin, J. Filipot, R. Magne, A. Roland, A. van der Westhuysen, P.  
544 Queffeulou, J.M. Lefevre, L. Aouf, F. Collard, “Semi-empirical dissipation source functions for ocean  
545 waves. Part I: Definition, calibration, and validation”. *Journal of Physical Oceanography*, 40(9):1917–1941,  
546 2010.

547 25 A. Bentamy, D. Croizé. Fillon, “Gridded Surface Wind Fields from  
548 Metop/ASCAT Measurements”, *International Journal of Remote Sensing*, 33:  
549 1729-1754, 2011.

550 26 Courants de marée et hauteurs d’eau. La Manche de Dunkerque à Brest. Service Hydrographique et  
551 Océanographique de la Marine, Brest, Rapport 564-UJA, 2000

552 27 Tong, H. *Non-linear time series, a dynamical systems approach*. Oxford University Press, 1990.

553 28 J. P. Hughes and P. Guttorp. “A Class of Stochastic Models for Relating Synoptic Atmospheric  
554 Patterns to Regional Hydrologic Phenomena”, *Water Resources Research*, 30, 1535-1546, 1994a.

- 555           29 J. P. Hughes and P. Guttorp, “Incorporating Spatial Dependence and Atmospheric Data in a Model  
556 of Precipitation”. *Journal Applied Meteorology*, 33, 1503-1515, 1994b.
- 557           30 A.P. Dempster, N.M. Laird and D.B. Rubin, “Maximum likelihood from incomplete data via the EM  
558 algorithm”, *Journal of the Royal Statistical Society. Series B (Methodological)*, 39, 1–38, 1977.
- 559           31 F. Castino, R. Festa, and C.F. Ratto, “Stochastic modelling of wind velocities time series”, *Journal of*  
560 *Wind*
- 561           32 W. Zucchini and P. Guttorp. “A hidden Markov model for space-time precipitation”, *Water*  
562 *Resources Research*, 27, 1917–1923, 1991.
- 563           33 O. Cappe, E. Moulines, and T. Ryden. “Inference in hidden Markov models”. Springer-Verlag, New  
564 York, 2005.
- 565           34 H.S. Bhat, N. Kumar, “On the derivation of the Bayesian Information Criterion”, 2010, Available  
566 from <http://nscs00.ucmerced.edu/~nkumar4/BhatKumarBIC.pdf>.
- 567           35 B. Saulquin, F. Gohin, R Garrello, “Regional objective analysis for merging high-resolution MERIS,  
568 MODIS/Aqua, and SeaWiFS chlorophyll-a data from 1998 to 2008 on the European Atlantic shelf”, *IEEE*  
569 *Trans Geoscience Remote Sensing* 49(1), 143–154, 2011.
- 570           36 H.L. Tolman. “A mosaic approach to wind wave modeling”. *Ocean Modell*, 25(1/2), 35–47, 2008.
- 571           37 B. Saulquin, R. Fablet, A. Mangin, G. Mercier, D. Antoine, and O. Fanton d'Andon, “Detection of  
572 linear trends in multisensor time series in the presence of autocorrelated noise: Application to the  
573 chlorophyll-a SeaWiFS and MERIS data sets and extrapolation to the incoming Sentinel 3-OLCI mission”,  
574 *Journal of Geophysical Research Oceans*, 118, 3752–3763, 2013.
- 575           38 H. Schiller, R. Doerffer, “Neural network for emulation of an inverse model operational derivation  
576 of Case II water properties from MERIS data”. *International Journal of Remote Sensing*, 20(9), 1735-1746,  
577 1999.

578           39 B. Saulquin, A. Hamdi, F. Gohin, J. Populus, A. Mangin, O. Fanton D'Andon, "Estimation of the  
579 diffuse attenuation coefficient K-dPAR using MERIS and application to seabed habitat mapping". Remote  
580 Sensing Of Environment, 128, 224-40

581